J. Fluid Mech. (2006), *vol.* 548, *pp.* 69–86.
doi:10.1017/S002211200500741X Printed in the United Kingdom

Breakup time and morphology of drops and bubbles in a high-Reynolds-number flow

By J. RODRÍGUEZ-RODRÍGUEZ[1], J. M. GORDILLO[2] AND C. MARTÍNEZ-BAZÁN[1]†

[1]Departamento de Ingeniería Térmica y de Fluidos, Universidad Carlos III de Madrid, Avda. de la Universidad 30, 28911, Leganés, Madrid, Spain
fjrodriguez@ucsd.edu

[2]Área de Mecánica de Fluidos, Departamento de Ingeniería Energética y Mecánica de Fluidos, Universidad de Sevilla. Avda. de los Descubrimientos s/n, 41092, Sevilla, Spain
jgordill@us.es

(Received 14 March 2005 and in revised form 21 July 2005)

The breakup process of a drop or a bubble immersed in a straining flow at high Reynolds numbers, is studied numerically with the aim at comparing the breakup frequencies obtained with those measured in real flows. We assume that both the inner and the outer velocity fields are axisymmetric and irrotational. Under these assumptions the time evolution of the drop's interface is computed with a boundary integral method for a wide range of the inner-to-outer density ratios, Λ. Despite the simplicity of the model, it qualitatively displays some of the features of the turbulent breakup of drops and bubbles observed experimentally. Furthermore, when $\Lambda \sim O(1)$, the slender geometry of the droplets observed in the numerical simulations suggests the use of a simplified theoretical analysis that reproduces accurately the time evolution of the drop radius obtained numerically.

1. Introduction

Although desirable, numerical simulations of the turbulent breakup of drops and bubbles would be extremely expensive in terms of computing time owing to the wide range of length scales and unsteadiness that characterizes turbulence, in addition to the intrinsic difficulty of accounting for the presence of highly distorted three-dimensional free surfaces within the computational domain. As a first simplification, we propose a model that, retaining some important physical aspects of turbulent breakup, may help to understand the complexity of the process. The leading ideas are suggested by a careful examination of high-speed video images similar to those depicted in figure 1 and 2, taken from the experiments described in Rodríguez-Rodríguez (2004) and Eastwood, Armi & Lasheras (2004), respectively. The pictures illustrate the morphology of the turbulent breakup of a bubble and a heptane drop under well-controlled experimental conditions. Analysis reveals that the bubble in figure 1(a, b), whose initial shape is roughly spherical, is elongated in a preferential direction in figure 1(c, d). Finally, the breakage takes place sometime between figures 1(e) and 1(f), when the aspect ratio of the bubble is about 2.4. Similarly, figure 2

† Present address: Área de Mecánica de Fluidos. Departamento de Ingeniería Mecánica y Minera, Universidad de Jaén, Campus de las Lagunillas, 23071, Jaén, Spain; cmbazan@ujaen.es

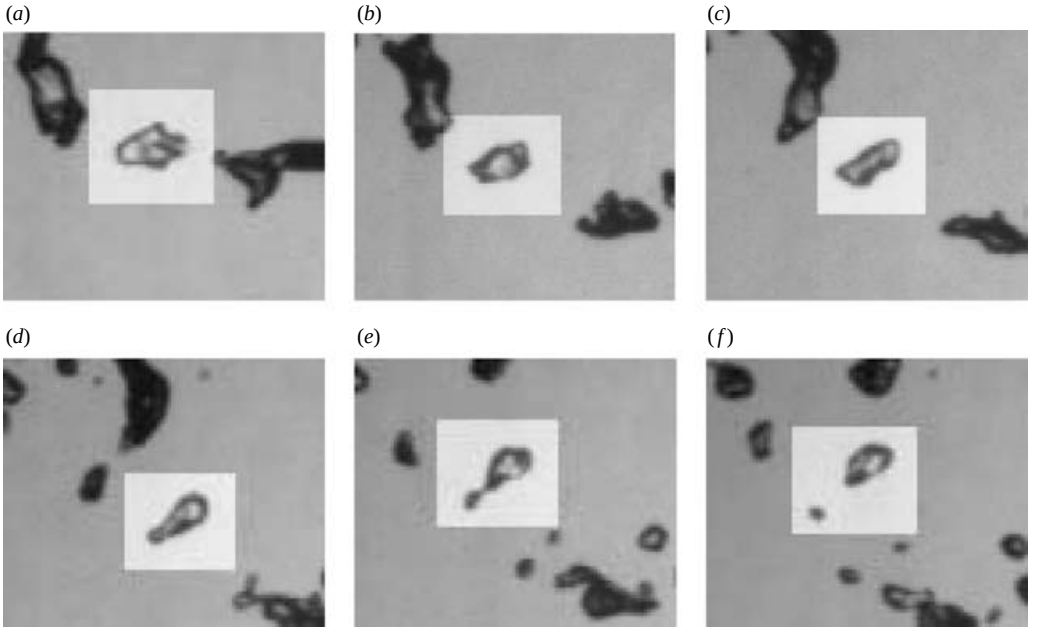

FIGURE 1. High-speed video images, recorded at 1000 f.p.s., of the slender breakage of an air bubble injected at the centreline of a turbulent water jet. Here, the diameter of the bubble is $2a_0 = 2.5\,\mathrm{mm}$, the dissipation rate of turbulent kinetic energy is $\varepsilon = 62\,\mathrm{m^2\,s^{-3}}$, providing a Reynolds number $Re \simeq 780$ and a mean Weber number $\langle We \rangle \simeq 10$, following the definition given by equation (3.2).

shows that the initially round heptane drops deform into slender ligaments before pinching-off. Therefore, the kind of breakup process displayed in figures 1 and 2 can be classified, according to the classical work of Hinze (1955), as a *cigar shaped* type of breakup. The observation of these images allows us to infer that the particle breaks up because of its interaction with turbulent eddies of the same size which stretch the particle before breaking up, as already indicated in the Kolmogorov–Hinze theory (Kolmogorov 1949; Hinze 1955). The observed stretching implies that there is a preferential direction along which deformation occurs and, thus, the breakup process can be assumed to be, in a first approximation, axisymmetric.

To further simplify the problem, we will consider that the particle is moving at the local mean fluid velocity and that its characteristic size, a_0, lies within the inertial subrange of the turbulent energy spectrum. This condition ensures that the Reynolds number based on the outer fluid properties of the flow surrounding the particle is sufficiently large for us to neglect viscous effects. Furthermore, in the case of droplets, we will also assume that the inner-to-outer kinematic viscosity ratio is, at the most, of order unity, indicating that the Reynolds number of the inner flow is also large. For instance, in figure 1, the Reynolds number based on the mean velocity difference between two points separated by a distance of the order of the particle radius, $u'(a_0)$, is $Re_{a_0} = u'(a_0)a_0/\nu \approx 780$. Similarly, that of figure 2, where the inner-to-outer kinematic viscosity ratio is 0.88, is $Re_{a_0} \approx 500$. Finally, an additional simplification adopted here will be to consider that both the inner and the outer flows are irrotational. Although strictly speaking the analysis of the instantaneous velocity field surrounding the

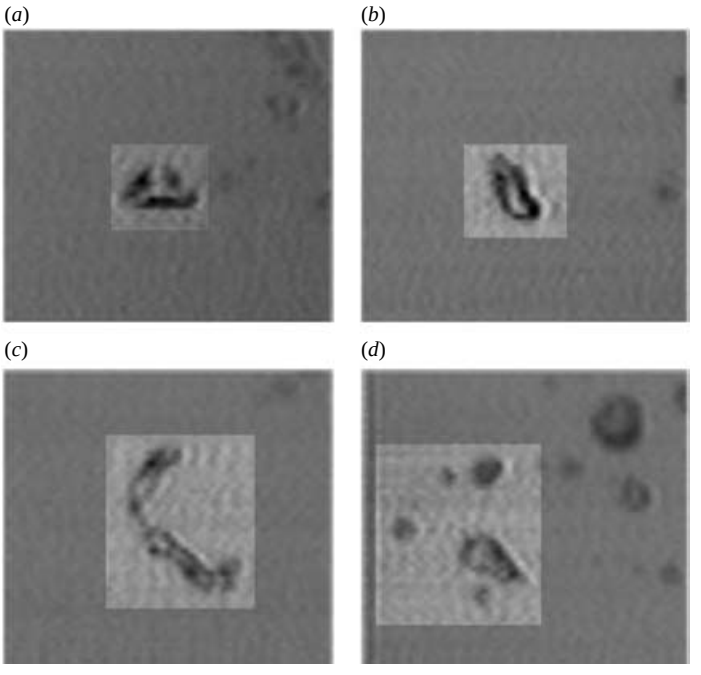

FIGURE 2. Breakup of a heptane droplet of 1.65 mm diameter immersed in a turbulent water flow. Here, the dissipation rate of turbulent kinetic energy is $\varepsilon = 84\,\mathrm{m^2\,s^{-3}}$, yielding for the Reynolds and mean Weber numbers the values $Re \simeq 500$ and $\langle We \rangle \simeq 10$, respectively. It can be observed that the drop is stretched, becoming a slender ligament in (*c*) before it breaks in (*d*). Images taken from the experiments described in Eastwood *et al.* (2004).

particle in real turbulent flows indicates that vorticity may not be negligible (Chong, Perry & Cantwell 1990; Perry & Chong 1993), as a first approach to the problem, in this work we will consider only the symmetric part of the velocity-gradient tensor (strain-rate tensor). Note that the strain-rate tensor assumed here properly models the outer flow as a stable focus, which is the most likely structure of the instantaneous velocity field in turbulent flows (Chong *et al.* 1990; Perry & Chong 1993). A more detailed analysis including the rotational tensor is left for a future work already in progress.

The description of the main features of the turbulent breakup of drops and bubbles using the potential flow approximation has been previously used by a number of authors. Shreekumar, Kumar & Gandhi (1996) studied the influence of a turbulent gas field on the breakup of a liquid drop, and modelled the turbulent velocity fluctuations as an unsteady pressure distribution along the drop surface. Kang & Leal (1987) considered the deformation of a bubble immersed in an uniaxial straining type of flow both at finite Reynolds numbers and under the potential-flow approximation. Although these authors find the critical Weber number above which no steady solutions exist imposing an outer flow similar to that adopted here, they do not provide the breakup time dependence on the parameters of the problem. Moreover, the interaction of a bubble with a turbulent structure has been considered by Higuera (2004), who studied the deformation of a gas bubble induced by the action of a vortex ring as a simple approach to model the bubble–turbulence interaction. In accordance

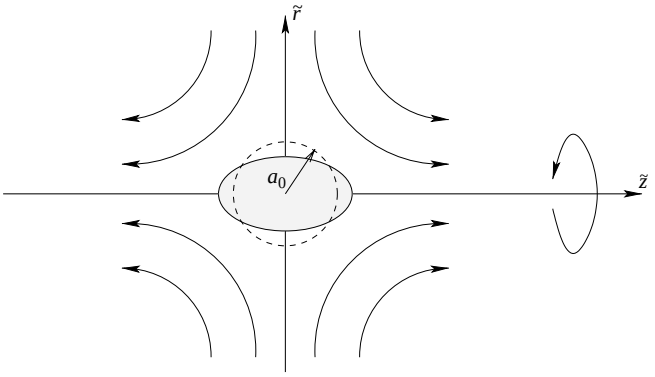

FIGURE 3. Sketch of the flow field under investigation. Here, $\tilde{r}$ and $\tilde{z}$ indicate the dimensional radial and axial coordinates.

with the Kolmogorov–Hinze hypothesis, Higuera (2004) concludes that the most efficient eddies are those whose size is similar to that of the particle. However, the breakup times obtained in his study strongly depend on the initial position of the vortex core and, unfortunately, this work does not supply significant information about the real dependence of the breakup time on the parameters of the problem. On the other hand, the numerical results presented here will provide the time evolution of the interface of an initially round immiscible particle, deformed owing to the action of a steady, axisymmetric and hyperbolic type of flow (figure 3). As already mentioned, the axisymmetry of the imposed outer velocity field is motivated by experimental observations similar to those depicted in figures 1 and 2, where the particle's interface is elongated in a preferential direction. Similarly, figures 1 and 2 also suggest that the particle breaks owing to its interaction with a single turbulent structure whose characteristic turnover time is larger than the breakup time; hence, the additional simplification of considering the outer flow as steady is satisfied.

The paper is structured as follows. In § 2, both the formulation of the equations and boundary conditions governing the free-surface potential flow under study and the description of the boundary-element numerical method used to solve them is provided. Results concerning bubble breakup are discussed and compared with some experimental data in § 3, whereas the drop breakup problem and the analysis of the slender simplified model is left to § 4. Finally, conclusions are presented in § 5.

2. Problem formulation and numerical method

We will describe the time evolution of the interface of an immiscible drop (bubble) of density ρ_i and initial radius a_0, immersed into an infinite volume of a different fluid of density ρ_e. As stated before, we will consider that the drop (bubble) is moving at the local mean velocity of the flow and that both inner and outer flows are irrotational. In a frame of reference moving at the particle's velocity, the outer velocity field far from its interface is the hyperbolic, axisymmetric and steady flow given by the following dimensional velocity potential,

$$\Phi_e = \frac{M}{a_0}(-\tilde{r}^2 + 2\tilde{z}^2), \tag{2.1}$$

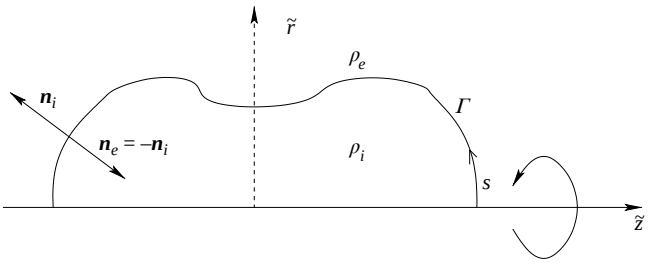

FIGURE 4. Definition of the variables used in the numerical method. Here, $\tilde{r}$ and $\tilde{z}$ indicate the dimensional radial and axial coordinates.

where M is the flow intensity and $(\tilde{r}, \tilde{z})$ are the radial and axial coordinates, respectively. A sketch of the suggested flow configuration is given in figure 3. Scaling the distances, times and densities with a_0, $a_0/8M$ and ρ_e respectively, the dimensionless equations governing the inner and outer potential flows are

$$\nabla^2 \phi_{(i,e)} = 0, \tag{2.2}$$

$$\Lambda\left(\frac{\partial \phi_i}{\partial t} + \frac{|\nabla \phi_i|^2}{2}\right) + p_i = P_{0i}, \qquad \frac{\partial \phi_e}{\partial t} + \frac{|\nabla \phi_e|^2}{2} + p_e = P_{0e}, \tag{2.3}$$

where the subscripts (i, e) refer to the inner and external fluid, respectively. Here, (2.2) are the Laplace equations for the velocity potentials $\phi_{i,e}$, (2.3) are the Bernoulli equations and $\Lambda = \rho_i/\rho_e$. Moreover, $P_{0(i,e)}$ are functions of time which, in this problem, can be set to zero since they can be included in the definitions of $\phi_{(i,e)}$ without affecting the velocity fields. The solution to equations (2.2) and (2.3) must be axisymmetric

$$\frac{\partial \phi_{(i,e)}}{\partial r} = 0 \quad \text{at} \quad r = 0, \tag{2.4}$$

and solved subjected to the following boundary conditions

$$\phi_e \to \phi_{e\infty}(r, z) = -r^2/8 + z^2/4 \text{ for } \quad (r, z) \to \infty \tag{2.5}$$

and

$$p_i - p_e = \frac{1}{We}\nabla \cdot \boldsymbol{n_i}, \tag{2.6}$$

$$\frac{\partial \phi_i}{\partial n_i} = -\frac{\partial \phi_e}{\partial n_e}, \tag{2.7}$$

at the surface of the drop (bubble). In equation (2.7), n_i and n_e are the inner and outer coordinates normal to the interface (figure 4), and $We = \rho_e(8M)^2 a_0/\sigma$ is the Weber number based on the drop's (bubble's) radius a_0, the outer flow characteristic velocity $8M$, and interfacial tension coefficient, σ. The time evolution of the particle's interface will be obtained by solving equations (2.2)–(2.7) with the boundary integral method described in the following subsection.

2.1. *Numerical method*

Free-boundary problems with large-amplitude or other non-trivial surface deformations generally require a numerical solution. To date, most of the solutions have focused on cases where only the dynamics of a single phase was important (e.g. an

oscillating gas bubble in water), however, in this paper we will consider the dynamics of two contiguous fluid domains. The basic ideas are similar to those exposed in a recent study of Leppinen & Lister (2003), who studied the dynamics near pinch-off using an alternative integral representation to the one described here. As a starting point, let us consider the Green's identity, which applied to both fluids provides integral equations for the velocity potentials $\phi_{(i,e)}$ at any given point $\boldsymbol{X}=(R, Z)$ on a smooth surface as a function of the potential distribution and its normal derivative to the surface, $\partial\phi_{(i,e)}/\partial n_{(i,e)}$,

$$\phi_{(i,e)}(R, Z) = \psi_{(i,e)}(R, Z) + \int_{\Gamma} \tilde{g}_{(i,e)} \frac{\partial \phi_{(i,e)}}{\partial n_{(i,e)}} \mathrm{d}s - \int_{\Gamma} \tilde{h}_{(i,e)} \phi_{(i,e)}\, \mathrm{d}s, \tag{2.8}$$

being $\psi_i(R, Z)=0$ and $\psi_e(R, Z)=2\phi_{e\infty}(R, Z)=-R^2/4+Z^2/2$. To derive this equation, axisymmetry has been assumed and integration along the azimuthal variable has been performed. Therefore, integrals in (2.8) are line integrals along a meridian of the free surface, denoted by Γ, s being the arclength (see figure 4). Note also that, as indicated in figure 4, normal vectors $\boldsymbol{n}_{(i,e)}$ are directed away from the inner/outer fluid domains. Kernel functions $\tilde{g}$ and $\tilde{h}$ in (2.8) are given by,

$$\left.\begin{aligned} \tilde{g}_{(i,e)} &= \frac{2r}{\pi \tilde{A}^{1/2}} K(\tilde{m}), \\ \tilde{h}_{(i,e)} &= \frac{2r E(\tilde{m})}{\pi \tilde{A}^{1/2}} \left[\frac{n^r_{(i,e)}}{2r} + \frac{(R-r)n^r_{(i,e)} + (Z-z)n^z_{(i,e)}}{\tilde{B}} \right] - \frac{K(\tilde{m}) n^r_{(i,e)}}{\pi \tilde{A}^{1/2}}, \end{aligned}\right\} \tag{2.9}$$

where $K(\tilde{m})$ and $E(\tilde{m})$ are the elliptic functions of the first and second kind, respectively,

$$\tilde{A} = (R+r)^2 + (Z-z)^2, \quad \tilde{B} = (R-r)^2 + (Z-z)^2, \quad \tilde{m} = \frac{4rR}{\tilde{A}}, \tag{2.10}$$

and $n^r_{(i,e)}$, $n^z_{(i,e)}$ are the projection of the normal vector to the inner (i) and outer (e) fluid boundaries in the radial (r) and axial (z) direction (see figure 4). Since both fluids share the same boundary, $\boldsymbol{n}_i=-\boldsymbol{n}_e$, indicating that

$$\tilde{g}_e = \tilde{g}_i, \quad \tilde{h}_e = -\tilde{h}_i. \tag{2.11}$$

The time evolution for the potentials $\phi_{(i,e)}$ is provided by the Bernoulli equations (2.3). Note first that the material derivative of $\phi_{(i,e)}$ along the normal to the surface ($\mathrm{D}^n/\mathrm{D}t$) is simply

$$\frac{\mathrm{D}^n \phi_{(i,e)}}{\mathrm{D}t} = \frac{\partial \phi_{(i,e)}}{\partial t} + \left(\frac{\partial \phi}{\partial n} \right)^2. \tag{2.12}$$

Defining the difference function

$$\varphi = \phi_e - \Lambda \phi_i, \tag{2.13}$$

equations (2.3) can be combined with the normal stress balance (2.6) to yield,

$$\frac{\mathrm{D}^n \varphi}{\mathrm{D}t} = \frac{1}{We} \nabla \cdot \boldsymbol{n}_i + \tfrac{1}{2}(1-\Lambda) \left(\frac{\partial \phi}{\partial n} \right)^2 - \tfrac{1}{2} \left[\left(\frac{\partial \phi_e}{\partial s} \right)^2 - \Lambda \left(\frac{\partial \phi_i}{\partial s} \right)^2 \right]. \tag{2.14}$$

Here, $\partial\phi_i/\partial s$ and $\partial\phi_e/\partial s$ are the derivatives along the free surface of the inner and outer potentials, respectively. In (2.12) and (2.14), we have used the free-surface kinematic condition (2.7) and we have omitted the subscript (i, e) when the result is independent of the use of the inner or outer variables.

The discretization of the integrals was performed as in Oguz & Prosperetti (1989, 1993) where the free-surface coordinates R and Z, the potentials $\phi_{(i,e)}$ and their normal derivative $\partial\phi_{(i,e)}/\partial n_{(i,e)}$, are defined at discrete boundary points. Quartic splines taking the arclength s as the spline parameter were used to interpolate the values of (R, Z) (Day, Hinch & Lister 1998). Furthermore, spline interpolation was also employed to calculate both the normal vectors and tangential derivatives, $\partial/\partial s$, of the potentials $\phi_{(i,e)}$. We also assumed that the unknowns of equation (2.8) varied linearly between nodal points in order to transform the integral equation into an algebraic linear system. Integrals in (2.8) were calculated by adding the contribution along each segment formed between two consecutive nodal points. The elliptic functions $E(\tilde{m})$ and $K(\tilde{m})$ were evaluated using the explicit formulae, with errors $O(10^{-8})$, provided in Abramowitz & Stegun (1970). The logarithmic singularity, which was introduced in the kernels $\tilde{g}$ and $\tilde{h}$ owing to the presence of the elliptic function $K(\tilde{m})$, was handled by finding an explicit expression for the logarithmic terms. After doing this, regular integrals were computed using the six-point Gauss–Legendre formula, while integrals containing logarithms were evaluated as described in Oguz & Prosperetti (1989). Therefore, computing $\partial\phi_{(i,e)}/\partial n_{(i,e)}$ from equation (2.8) was reduced to solving the following linear system

$$\left(\overline{\overline{I}} + \overline{\overline{\mathscr{H}}}_{(i,e)}\right)\boldsymbol{\Phi}_{(i,e)} \equiv \overline{\overline{H}}_{(i,e)}\boldsymbol{\Phi}_{(i,e)} = \boldsymbol{\Psi}_{(i,e)} + \overline{\overline{G}}_{(i,e)}\frac{\partial \boldsymbol{\Phi}_{(i,e)}}{\partial \boldsymbol{n}_{(i,e)}}, \tag{2.15}$$

where each of the elements of the vectors $\boldsymbol{\Phi}_{(i,e)}$, $\boldsymbol{\Psi}_{(i,e)}$ and $\partial\boldsymbol{\Phi}/\partial\boldsymbol{n}$ represent, respectively, the values of $\phi_{(i,e)}$, $\psi_{(i,e)}$ and $\partial\phi/\partial n$ at each nodal point, while $\overline{\overline{\mathscr{H}}}$ and $\overline{\overline{G}}$ are the matrices corresponding to the discretization of the integral operators of equation (2.8). In the implementation reported here, the nodal points of both the inner and outer fluids are placed at the same $\boldsymbol{X} = (R, Z)$ coordinates. Consequently, the addition of the equations corresponding to the inner and outer fluids in equation (2.15) leads to

$$\overline{\overline{H}}_i\boldsymbol{\Phi}_i + \overline{\overline{H}}_e\boldsymbol{\Phi}_e = 2\boldsymbol{\Phi}_{e\infty} \Rightarrow (\overline{\overline{H}}_i + \Lambda\overline{\overline{H}}_e)\boldsymbol{\Phi}_i = 2\boldsymbol{\Phi}_{e\infty} - \overline{\overline{H}}_e\varphi, \tag{2.16}$$

where use of the definition of φ in (2.13) and of equations (2.11) and (2.7), has been made. Once equation (2.16) has been deduced, the numerical algorithm is straightforward. The value of φ at a certain time step is worked out through (2.14). Then, the values of $\boldsymbol{\Phi}_i$ and $\boldsymbol{\Phi}_e$ are obtained from (2.16) and (2.13), respectively. On the other hand, the normal velocity is determined from one of the equations (2.15) using the already calculated value of $\boldsymbol{\Phi}_i$. The positions of the free-surface nodal points are advanced in time by moving them normal to the interface, so that for each node, we use the equations

$$\frac{\mathrm{d}R}{\mathrm{d}t} = n_i^r\frac{\partial\phi_i}{\partial n_i}, \quad \frac{\mathrm{d}Z}{\mathrm{d}t} = n_i^z\frac{\partial\phi_i}{\partial n_i}. \tag{2.17}$$

Then, equation (2.14) allows us to advance in time with φ and the cycle begins again. The temporal integration was performed using an explicit standard, adaptive fourth-order Runge–Kutta scheme. This scheme was chosen to solve properly the final stages before pinch-off occurs. In order to avoid the growth of high-frequency waves at the free surface, the different discrete functions were fast Fourier transformed at each time step and the higher modes eliminated; moreover, the nodal points were rearranged in order for them to be equispaced (Oguz & Prosperetti 1989, 1993). The linear system of algebraic equations (2.15)–(2.16) was solved using the LU decomposition method. As a validation test for the numerical procedure, the frequency of small oscillations

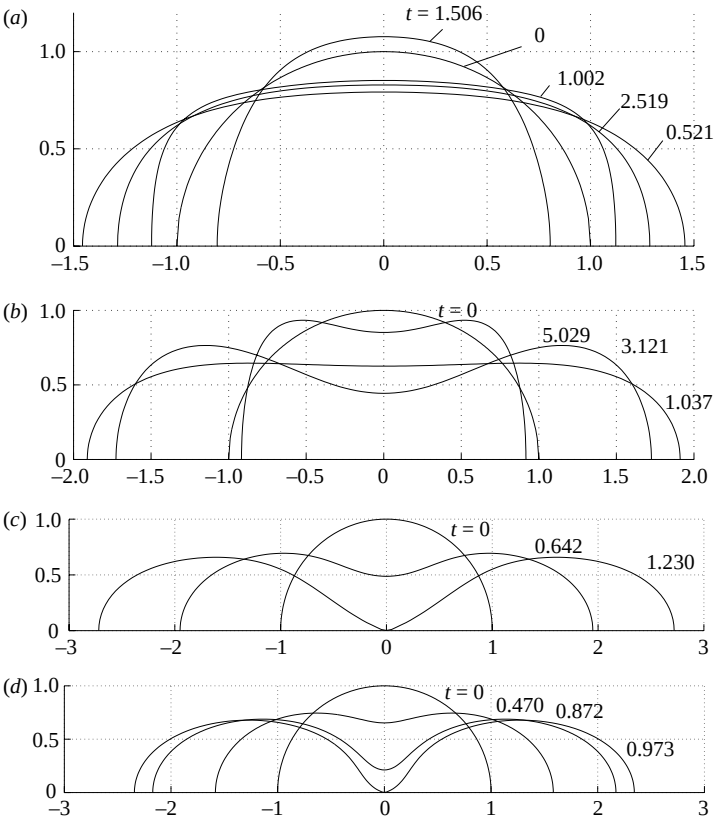

FIGURE 5. Time evolution of the breakup process of an air bubble in water ($\Lambda = 1.2 \times 10^{-3}$) for different values of the Weber number. (*a*) $We = 1.0$, (*b*) $We = 2.19$, (*c*) $We = 10.0$ and (*d*) $We \to \infty$.

of a nearly spherical drop was obtained for different values of Λ, and compared with the analytical results given by Lamb (1932). Using 65 nodes, the relative error was, for any value of Λ, always less than 0.5 % for the second mode of oscillation and less than 2 % for the fourth. Clearly, this error could be reduced if more nodal points were added. Therefore, we considered this test validated the proposed scheme.

3. Bubble breakup

The first problem, considered in this section, is the study of the breakup of a gas bubble immersed in an inviscid liquid flow. Note that, in this case, the density ratio is much smaller than unity, $\Lambda \ll 1$, and the only parameter governing the problem is the Weber number, *We*. Numerical simulations of the time evolution of the bubble's interface, performed for a wide range of Weber numbers, show that there are two different scenarios depending on the value of *We*. For Weber numbers smaller than the critical one, $We_c = 2.3$, the bubble oscillates indefinitely without breaking up. However, when $We > We_c$, the bubble splits into two fragments. The time evolution of the bubble for two subcritical cases ($We = 1.0$ and $We = 2.19$) is displayed in figures 5(*a*) and 5(*b*), respectively. Although in both cases the bubble oscillates indefinitely, the amplitude of the oscillations increases noticeably as the Weber number approaches We_c.

On the other hand, when $We > We_c$, the breakup morphology no longer depends on the Weber number, and the bubble always splits into two fragments (figures 5*c* and 5*d*).

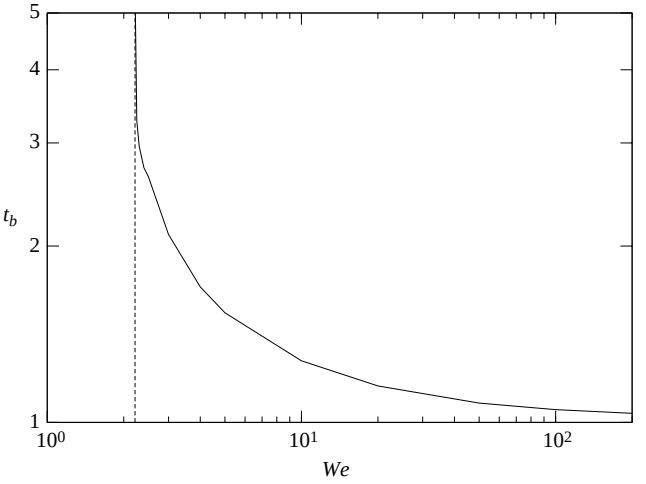

FIGURE 6. Dependence of the dimensionless breakup time of bubbles, t_b, on the Weber number.

This result is in agreement with previous experimental observations reported by Risso & Fabre (1998), Martínez-Bazán, Montañés & Lasheras (1999*a*, *b*) and Rodríguez-Rodríguez, Martínez-Bazán & Montañés (2003) among others. In fact, these authors concluded that breakup patterns leading to more than two fragments were rarely observed for moderately high Weber numbers. It can also be observed in figures 5(*c*) and 5(*d*), that the aspect ratio of the deformed bubble decreases for increasing Weber numbers owing to the fact that the time that the outer liquid flow has to separate the bubble ends decreases.

Notice that our simulations indicate that bubbles only break if the inertia of the outer fluid is sufficiently large to overcome the surface tension confinement stresses, $We > We_c$. However, the coherent interaction of unsteady vortical structures with the bubble can also break it even if $We < We_c$. This is caused by a succession of subcritical stretches that might increase the surface energy in this non-dissipative system, and can eventually lead to bubble breakup in subcritical flows (see Kang & Leal 1990; Risso & Fabre 1998). Consequently, the abrupt transition from permanent oscillation to bubble breakup obtained in our simulations is a consequence of the steadiness of the outer fluid flow adopted here. Despite this limitation, it will be shown that our approach is realistic, in the sense that it is able to reproduce the breakup frequencies in some experiments.

The dependence of the dimensionless breakup time on the Weber number, $t_b(We)$, has been represented in figure 6. This figure shows that $t_b \to \infty$ as $We \to We_c$ and that, for sufficiently high Weber numbers, t_b tends to a constant value. This asymptote is in accordance with the fact that, since surface tension effects are negligible in this limit, the only relevant time scale of the problem is the convective one. The function $t_b\,(We)$ has also been compared with experimental measurements of the breakup frequency of bubbles immersed in a turbulent and isotropic flow performed by Martínez-Bazán *et al.* (1999*a*) and Rodríguez-Rodríguez (2004) in different facilities. To compare the numerical results with the experimental measurements properly, it is necessary to provide a definition of the experimental Weber number consistent with that adopted in our model. To define the Weber number, $We = \rho_e(8M)^2 a_0 \sigma^{-1}$, we have selected the characteristic velocity, $\Delta u = 8M$, given by the velocity difference between the points

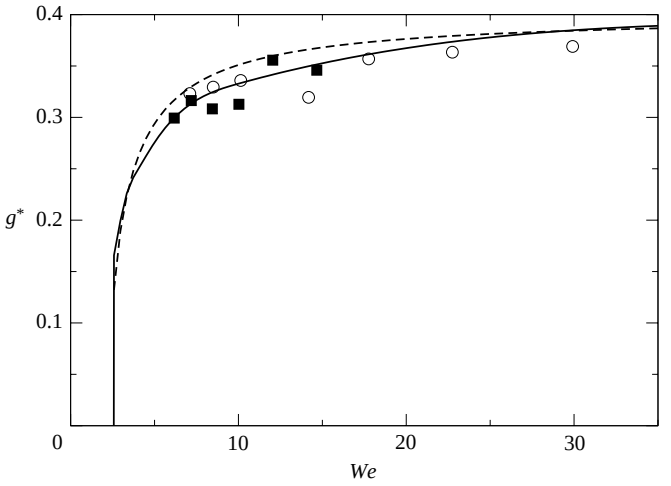

FIGURE 7. Comparison of the predicted breakup frequency (solid line) with the experimental measurements reported by Martínez-Bazán *et al.* (1999*a*) (circles) and Rodríguez-Rodríguez (2004) (squares) for air bubbles of $a_0 \approx 1.38$ mm and $a_0 \approx 2.00$ mm, respectively. In both experiments, the bubbles were injected at the axis of a submerged water jet. The dashed line corresponds to the breakup frequency given by equation (3.5).

$z = \pm a_0$ at the bubble axis. In a turbulent isotropic flow, this difference of velocity may be estimated as (Batchelor 1953),

$$\langle \Delta u^2 \rangle = C_K \varepsilon^{2/3} (2a_0)^{2/3}, \tag{3.1}$$

where ε is the dissipation rate of turbulent kinetic energy per unit mass and $C_K = 2.13$ is a numerical constant taken from Sreenivasan (1995). Thus, the turbulent Weber number can be given by,

$$\langle We \rangle = 3.38 \rho_e \varepsilon^{2/3} a_0^{5/3} \sigma^{-1}. \tag{3.2}$$

Similarly, since we are considering bubbles whose characteristic size lies within the inertial subrange of the turbulent energy spectrum, a proper scale for the convective time is given by

$$t_c \sim \varepsilon^{-1/3} a_0^{2/3}. \tag{3.3}$$

Consequently, the experimental dimensionless frequency, g^*, may be defined as

$$\langle g^* \rangle = \langle g \rangle \varepsilon^{-1/3} a_0^{2/3} = 1/(\beta t_b), \tag{3.4}$$

where g is the experimentally measured dimensional breakup frequency and β is an order unity constant that arises from the definition of the convective time in (3.3). To check if the model studied here is able to capture the mechanisms involved in the turbulent breakup of bubbles, we have plotted both the experimental data (symbols) and the numerical results (solid line) in figure 7. Notice the good agreement between the experimental measurements and the numerical results for the entire range of Weber numbers explored here, with only an order unity constant $\beta = 2.36$ to be adjusted. Furthermore, using equations (3.1) to (3.3) to make dimensionless the breakup frequency model proposed by Martínez-Bazán *et al.* (1999*a*) in their equation

(4.8), we obtain the following analytical expression,

$$\langle g^* \rangle = \frac{1}{\beta}\sqrt{1 - \frac{We_c}{\langle We \rangle}}. \tag{3.5}$$

The model for the breakup frequency given by equation (3.5) is a generalization of the phenomenological model for the breakup of a bubble in a turbulent flow proposed by Martínez-Bazán *et al.* (1999*a*, *b*). The main idea underlying this equation is that the breakup time (inverse of the breakup frequency) can be obtained using dimensional analysis. A time scale can be built with the density of the continuous phase, the radius of the bubble and the difference between the turbulent pressure fluctuation and the surface tension stresses, this difference being a measure of the energy available in the flow to split the bubble. The breakup frequency given by equation (3.5) has also been represented in figure 7 in the dashed line with $We_c = 2.3$. Note that the model agrees well with the numerical and the experimental results and, therefore, (3.5) can be used as an alternative expression to determine the bubble breakup frequency in practical applications.

In this section, we have provided a numerical model whose results compare fairly well with experiments even in the case of moderate Weber numbers. Thus, if in any particular case, the Weber number is consistently defined and the bubble size lies within the inertial subrange, the breakup time can be determined by means of this approach, avoiding the consideration of the more complex aspects of the flow.

4. Drop breakup

After the description of the breakup process of bubbles, in this section we will focus on the study of the effect of both the density ratio and the Weber number on the breakup of light drops, $\Lambda \leqslant 1$, at high Reynolds numbers. Unlike its low-Reynolds-number counterpart, the theoretical analysis of this problem has been overlooked in the literature in spite of its relevance for practical purposes. A comprehensive review of the literature about the deformation and breakup of drops subjected to a straining flow at zero Reynolds number is given by Stone (1994). The low-Reynolds-number breakup of drops of characteristic length smaller than the Kolmogorov scale has been studied by Cristini *et al.* (2003) in isotropic turbulent flows.

The main feature of the breakup process of light droplets given by our model is that two drops form symmetrically at both tips of an intermediate ligament (see figures 8*a* and 8*d*). It can also be observed that the form of the breakup near the pinch-point is that of a dimple/depression on a sphere (see Day *et al.* 1998; Leppinen & Lister 2003). Consequently, rather than a binary breakup observed for bubbles, droplets exhibit a tertiary breakup whenever the Weber number is higher than a critical value. The size of the central ligament strongly depends on both the Weber number and the density ratio. Figures 8(*a*) and 8(*c*), indicate that when the Weber number is slightly higher than the critical one, the drop breaks into two big daughter droplets and a small satellite. However, for larger values of the Weber number, two different scenarios may appear: at low values of Λ the volume of the satellite still remains small (see figure 8*b*), whereas if the density ratio is close to unity, $\Lambda \sim O(1)$, the drop elongates considerably, generating a slender ligament whose length, l, is much larger than its radius, a, $l/a \gg 1$, by the time it breaks (see figure 8*d*). This last type of breakup pattern has also been experimentally observed in the turbulent breakup of heptane drops ($\Lambda \simeq 0.7$) at high Reynolds numbers. As an example, figure 2,

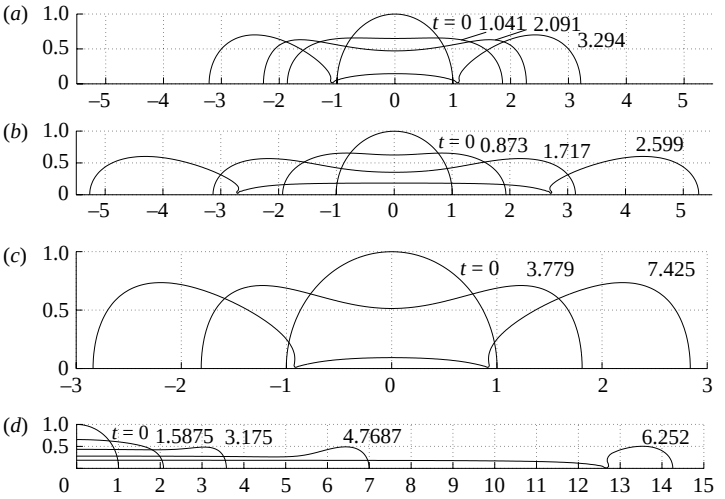

FIGURE 8. Time evolution of the breakup process of a drop for different values of the *We* and Λ. (*a*) $We = 3.0$ and $\Lambda = 0.20$, (*b*) $We = 10.0$ and $\Lambda = 0.20$, (*c*) $We = 3.0$ and $\Lambda = 0.80$, (*d*) $We = 10.0$ and $\Lambda = 0.80$. In the last case, only half of the droplet is shown.

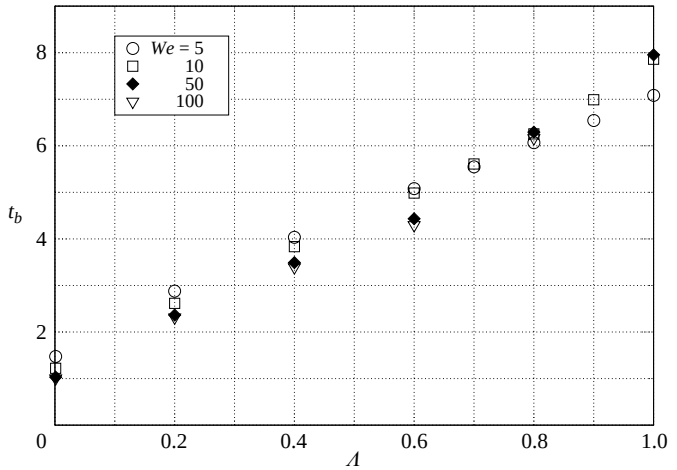

FIGURE 9. Dependence of the breakup time, t_b, on Λ for several values of *We*.

taken from Eastwood *et al.* (2004), shows how a heptane droplet is stretched by the surrounding flow until it is long enough to develop a capillary pinch-off of the ligament. The similarity between experimental and numerical observations lead us to the conclusion that the elongation prior to the subsequent breakup of the drop is driven by inertial and surface-tension forces. Thus, although viscous effects may affect the breakup frequency (Eastwood *et al.* 2004), the large elongation suffered by the droplets can be attributed to the inner fluid inertia.

Figure 9 shows the dependence of the breakup time, t_b, on Λ for several values of *We*. It can be seen that, since for sufficiently high values of the Weber number the relevant time scale of the problem is the convective one, the dependence of t_b on *We* is very weak when $We \gtrsim 5$. This figure also depicts an almost linear dependence of t_b on Λ. Figure 10 shows the dependence of the critical Weber number on Λ,

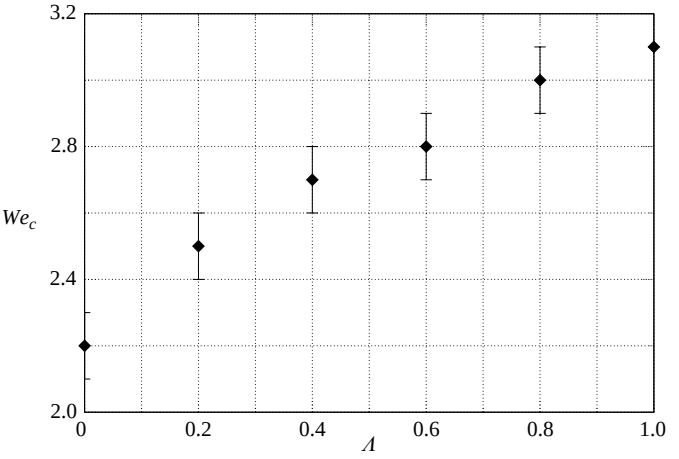

FIGURE 10. Critical Weber number dependence on the density ratio, Λ.

indicating that as the density of the inner fluid increases, the outer fluid inertia must also increase to split the particle.

However, unlike in the case of bubbles, the droplets elongate owing to their interaction with the outer flow and adopt the form of a long ligament that turns around itself, as displayed in experiments reported by Eastwood *et al.* (2004). Thus, the length of the ligament may become larger than the integral scale of the surrounding turbulent flow (or equivalently much larger than the breaking eddy) before it breaks (see figure 8*d*). This implies that, in those situations, the local velocity field given by equation (2.1) no longer applies, invalidating the approach considered here and the characteristic time of the problem given by (3.3). Also, as discussed in Eastwood *et al.* (2004), the inner fluid viscosity, not included in our model, plays an essential role during the latest instants of drop breakup. In view of these results, it can be concluded that, although our numerical approach is not appropriate for predicting either the experimentally measured breakup frequency or the critical Weber number, it qualitatively reproduces the observed breakup patterns. Thus, the following analytical model has been developed to describe the time evolution of a droplet before it breaks.

4.1. *Analytical model for the time evolution of slender drops and analysis of the local behaviour near pinch-off of drops*

As shown in figure 8(*d*), after a short initial transient, the drop deforms into a slender ligament whose radius, $a(t)$, slowly varies along the z-axis, except in a region close to the ends. These numerical (and experimental) observations suggest modelling the drop as a constant volume cylinder whose radius, $a(t)$, and length, $l(t)$ vary with time. Under this assumption, the solution of the Laplace equations (2.2) subjected to the boundary conditions (2.4), (2.5) and (2.7), gives the following inner and outer velocity fields

$$\phi_{e,r} = \tfrac{1}{4}\left(-r + \frac{a(t)^2}{r}\right) + \frac{a(t)\dot{a}(t)}{r}, \quad \phi_{e,z} = \tfrac{1}{2}z \quad \text{for} \quad r > a(t), \tag{4.1}$$

$$\phi_{i,r} = \frac{\dot{a}(t)}{a(t)}r, \quad \phi_{i,z} = -\frac{2\dot{a}(t)}{a(t)}z \quad \text{for} \quad r < a(t). \tag{4.2}$$

In equations (4.1)–(4.2), the subscripts r and z indicate partial derivation with respect to the radial (r) and longitudinal (z) coordinates, respectively. Notice that the normal

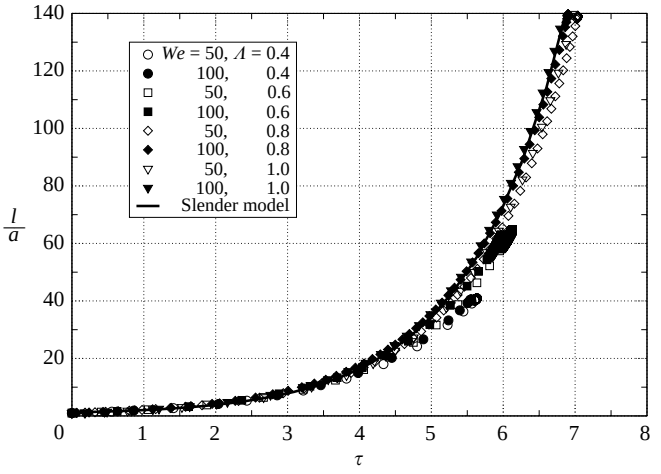

FIGURE 11. Time evolution of the ligament's aspect ratio obtained from numerical simulations for different values of Λ and We together with the evolution given by equation (4.5).

stress jump condition,

$$p_i\,(r=a,z,t)-p_e\,(r=a,z,t)=\frac{1}{We\,a(t)}, \tag{4.3}$$

imposes that the pressure difference across the interface, $p_i - p_e$, does not depend on z. Hence, substituting the velocity fields (4.1)–(4.2) into equations (2.3), and equating to zero the z-dependent term that results from subtracting the two Bernoulli equations (2.3), we obtain the following equation for $a(t)$

$$\frac{\ddot{a}}{a}-3\frac{\dot{a}^2}{a^2}+\frac{1}{8\Lambda}=0. \tag{4.4}$$

In terms of the scaled variable, $\tau = t/\sqrt{\Lambda}$, the solution of equation (4.4) subjected to the initial conditions $a(\tau=0)=1$, $\mathrm{d}a/\mathrm{d}\tau(\tau=0)=a_0'$ yields,

$$a(\tau)=\frac{\sqrt{2}\exp(-\tau/4)}{\sqrt{(1+4a_0')\exp(-\tau)+(1-4a_0')}}. \tag{4.5}$$

This simple model has been validated by comparing the time evolution of the drop aspect ratio $l/a = 1/a^3$, where $a(\tau)$ is given by equation (4.5), with that obtained from our simulations. Figure 11 shows that the numerical results, obtained for a wide range of We and Λ, closely follow the analytical prediction with $a_0' = -0.19$. The freedom in the choice of the initial condition a_0' comes from the non-slender geometry of the droplet during the initial stages of the breakup process.

Equation (4.4) is a generalization of a previous equation proposed by Frankel & Weihs (1985), who studied a similar problem to that considered where, unlike in our case, the outer fluid inertia was neglected. Indeed, letting $\Lambda \to \infty$ in (4.4), gives

$$a(t)=\frac{a_0}{\sqrt{\alpha t+1}}, \tag{4.6}$$

which coincides with the solution already obtained by Frankel & Weihs (1985).

The result shown in figure 11 also indicates that the stretching time scales with the square root of Λ, a dependence that results from the balance between inner to outer

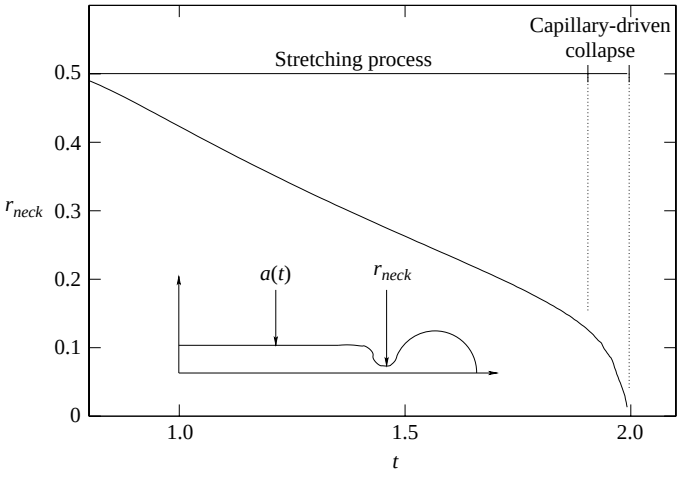

FIGURE 12. Illustration of the two stages observed in the collapse of the neck formed near the tips of the ligament.

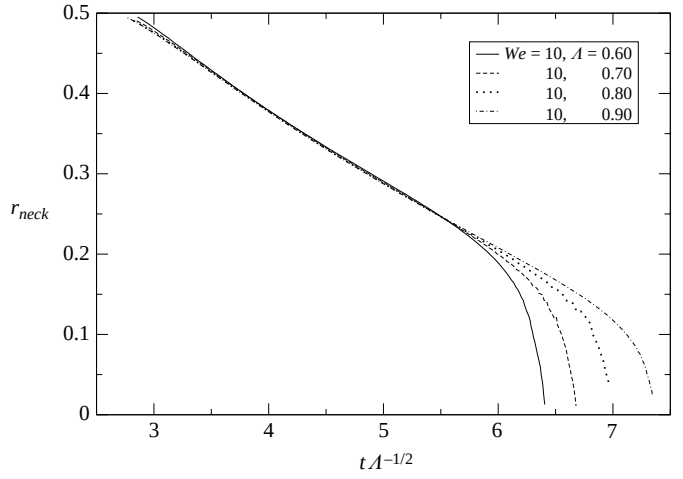

FIGURE 13. Final collapse of the neck for a fixed Weber number and different values of Λ. Notice that the inertial stage of the collapse increases with Λ.

fluid inertia: $\rho_i \ddot{a} a \sim \rho_e (8M)^2$. However, note that as indicated above, the breakup time depends almost linearly on Λ (see figure 9). This different trend may be explained by noticing that the breakup process can be divided into two separated stages: an inertial stage, in which the drop stretches as described by the previous model, and a capillary-driven pinch-off, similar to that proposed by Leppinen & Lister (2003) and Day *et al.* (1998). Figure 12 shows the evolution of the radius of the neck that forms when the ligament begins to collapse. As displayed in this figure, the capillary-driven stage is much shorter than the inertial one. Consequently, if the transition between both regimes occurred always at a fixed, dimensionless time τ_c, independent of Λ, the breakup time would scale as $\Lambda^{1/2}$. However, as depicted in figure 13, τ_c increases with Λ explaining the differences between the scaling of the stretching and the breakup processes.

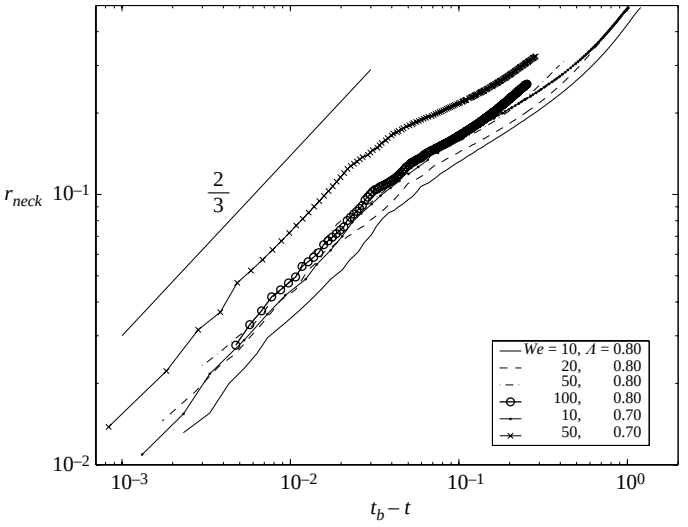

FIGURE 14. Evolution of the neck radius for several values of We and Λ showing that it follows the two-thirds law proposed by Day *et al.* (1998) and Leppinen & Lister (2003).

Moreover, to show that our numerical code describes the final stages of pinch-off properly, we have represented in figure 14 the evolution of the radius of the neck of drops [$\Lambda \sim O(1)$] with $t_b - t$, where t_b is the breakup time. This figure shows that, in agreement with the results provided in Chen & Steen (1997), Day *et al.* (1998) and Leppinen & Lister (2003), $r_{neck} \propto (t_b - t)^{2/3}$ which constitutes an additional proof of the accuracy of the present numerical code to simulate the potential two-phase flows considered in this paper.

As a final remark, note that drop dynamics near pinch-off is universal, in the sense that breakup at those scales is governed by a local balance of liquid inertia and surface tension. The drop radius profile near the singularity is locally self-similar, cone-shaped and strongly asymmetric, independently of initial or far-field flow conditions, as reported by Chen & Steen (1997), Day *et al.* (1998) and Leppinen & Lister (2003). Universality of drop breakup, and the largely asymmetrical structure of drop radius near pinch-off is the reason underlying satellite formation observed in experiments and numerical simulations (Eggers 1997, 2005). Nonetheless, these conclusions cannot be applied directly to bubble pinch-off at high Reynolds numbers, which is an open problem currently under study (Leppinen & Lister 2003; Burton, Waldrep & Taboreck 2005; Gordilla *et al.* 2005).

5. Conclusions

In this paper, we have reproduced some of the features of the breakup of a drop or a bubble in a homogeneous and isotropic turbulent flow under the potential flow approximation, assuming that, as suggested by Hinze (1955), the outer flow pattern may be modelled as an axisymmetric hyperbolic type of flow. In the case of bubbles, the breakup time predicted by the numerical model agrees well with the experimental measurements given in Martínez-Bazán *et al.* (1999*a*) and Rodríguez-Rodríguez (2004), once the Weber number and the correct time scale are properly defined. In addition, the asymptotic dependence of the breakup time on the Weber number is reached for considerably low values of this parameter, $We \sim 5$.

This constitutes a relevant result since it is the order of magnitude of the Weber number in many practical applications such as atomization processes. However, a limitation of the proposed model is that, at this point, our numerical approach is unable to predict the explosive breakup caused by the interaction of a particle with small-scale turbulent structures at high Weber numbers. Our simplified model is not appropriate for describing the breakup mechanism reported by Risso & Fabre (1998), who convincingly showed that the breakage of a bubble can also be induced by the resonant interaction of vortical unsteady structures with the particle. As described in Risso & Fabre (1998), this type of breakup is likely to occur when the characteristic capillary time is of the order of the turnover time of the turbulent structures interacting with the particle.

The role the inner fluid density plays in the breakup process has also been investigated. A first result of interest, which agrees with the experimental observations provided by Eastwood *et al.* (2004), is that, if the inner and outer fluid densities are comparable, the drop deforms into a slender ligament that ultimately breaks up owing to capillary effects. Furthermore, our numerical simulations show that the breakup process can be divided in two different stages: a long, inertial phase, which essentially determines the duration of the process; and a shorter capillary-driven stage that ultimately leads to the collapse of the particle.

Finally, a simple analytical model that accurately reproduces the numerically obtained time evolution of the drop radii in the cases of $We \gg 1$ and $\Lambda \sim O(1)$ has also been developed.

The authors wish to thank Dr C. D. Eastwood for providing experimental evidence of the breakage of heptane drops as well as Professor A. L. Sánchez for his valuable suggestions. The talks with Professor Howard A. Stone while the numerical code was being developed, and his help in the writing of § 2.1, are also greatly acknowledged. The authors would also like to thank the referees for their valuable and insightful comments, which have led to an improvement of the original version of the manuscript. This research has been partly supported by the Fifth Framework Programme of the European Commission under the Energy, Environment and Sustainable Development Contract EVG1-CT-2001-00042 EXPRO and by the Spanish MCyT under Project DPI2002-04550-C07-06. J. M. G. thanks the Spanish MCyT for the support of a post-doctoral grant during his stay at Harvard University.

REFERENCES

Abramowitz, M. & Stegun, I. A. 1970 *Handbook of Mathematical Functions*. Dover.

Batchelor, G. K. 1953 *The Theory of Homogeneous Turbulence*. Cambridge University Press.

Burton, J., Waldrep, R. & Taboreck, P. 2005 Scaling instabilities in bubble pinch-off. *Phys. Rev. Lett.* **94**, 184502.

Chen, Y. & Steen, P. 1997 Dynamics of inviscid capillary breakup: collapse and pinchoff of a film bridge. *J. Fluid Mech.* **341**, 245–267.

Chong, M. S., Perry, A. E. & Cantwell, B. J. 1990 A general classification of three-dimensional flow fields. *Phys. Fluids* A **2**, 765–777.

Cristini, V., Blawzdziewicz, J., Loewenberg, M. & Collins, L. R. 2003 Breakup in stochastic Stokes flows: sub-Kolmogorov drops in isotropic turbulence. *J. Fluid Mech.* **492**, 231–250.

Day, R. F., Hinch, E. J. & Lister, J. R. 1998 Self-similar capillary pinchoff of an inviscid fluid. *Phys. Rev. Lett.* **80**, 704–707.

Eastwood, C. D., Armi, L. & Lasheras, J. C. 2004 The breakup of immiscible fluids in turbulent flows. *J. Fluid Mech.* **502**, 309–333.

Eggers, J. 1997 Nonlinear dynamics and breakup of free surface flows. *Rev. Mod. Phys.* **69**, 865–929.

Eggers, J. 2005 Drop formation – an overview. *Z. Angew Math. Mech.* **85**, 400–410.

Frankel, I. & Weihs, D. 1985 Stability of a capillary jet with linearly increasing axial velocity (with application to shaped charges). *J. Fluid Mech.* **155**, 289–307.

Gordilla, J. M., Sevilla, A., Rodríguez-Rodríguez, J. & Martínez-Bazán, C. 2005 Axisymmetric bubble pinch-off at high Reynolds numbers. *Phys. Rev. Lett.* **95**, 194501.

Higuera, F. J. 2004 Axisymmetric inviscid interaction of a bubble and a vortex ring. *Phys. Fluids* **16**, 1156–1159.

Hinze, J. O. 1955 Fundamentals of the hydrodynamics mechanisms of splitting in dispersion process. *AIChE J.* **1**, 289–295.

Kang, I. S. & Leal, L. G. 1987 Numerical solution of axisymmetric, unsteady free-boundary problems at finite reynolds number. I. Finite-difference scheme and its application to the deformation of a bubble in a uniaxial straining flow. *Phys. Fluids* **30**, 1929–1940.

Kang, I. S. & Leal, L. G. 1990 Bubble dynamics in time-periodic straining flows. *J. Fluid Mech.* **218**, 41–69.

Kolmogorov, A. N. 1949 On the breakage of drops in a turbulent flow. *Dokl. Akad. Nauk. SSSR* **66**, 825–828.

Lamb, H. 1932 *Hydrodynamics*. Cambridge University Press.

Leppinen, D. & Lister, J. R. 2003 Capillary pinch-off in inviscid fluids. *Phys. Fluids* **15**, 568–578.

Martínez-Bazán, C., Montañés, J. L. & Lasheras, J. C. 1999*a* On the breakup of an air bubble injected into a fully developed turbulent flow. Part 1. Breakup frequency. *J. Fluid Mech.* **401**, 157–182.

Martínez-Bazán, C., Montañés, J. L. & Lasheras, J. C. 1999*b* On the breakup of an air bubble injected into a fully developed turbulent flow. Part 2. Size PDF of the resulting daughter bubbles. *J. Fluid Mech.* **401**, 183–207.

Oguz, H. N. & Prosperetti, A. 1989 Surface-tension effects in the contact of liquid surfaces. *J. Fluid Mech.* **203**, 149–171.

Oguz, H. N. & Prosperetti, A. 1993 Dynamics of bubble growth and detachment from a needle. *J. Fluid Mech.* **257**, 111–145.

Perry, A. E. & Chong, M. S. 1993 *Eddy Structure Identification in Free Turbulent Shear Flows* (ed. J. P. Bonnet & M. N. Glauser). Kluwer.

Risso, F. & Fabre, J. 1998 Oscillations and breakup of a bubble immersed in a turbulent field . *J. Fluid Mech.* **372**, 323–355.

Rodríguez-Rodríguez, J. 2004 *Estudio de la rotura de gotas y burbujas en flujos a altos números de Reynolds*. PhD thesis Universidad Carlos III de Madrid, Madrid.

Rodríguez-Rodríguez, J., Martínez-Bazán, C. & Montañés, J. L. 2003 A novel particle tracking and breakup detection algorithm: application to the turbulent breakup of bubbles. *Meas. Sci. Technol.* **14**, 1328–1340.

Shreekumar, R., Kumar, R. & Gandhi, K. S. 1996 Breakage of a drop of inviscid fluid due to a pressure fluctuation at its surface. *J. Fluid Mech.* **328**, 1–17.

Sreenivasan, K. R. 1995 On the universality of the Kolmogorov constant. *Phys. Fluids* **11**, 2778–2784.

Stone, H. A. 1994 Dynamics of drop deformation and breakup in viscous fluids. *Annu. Rev. Fluid Mech.* **26**, 65–102.